EXPERIMENTAL AND NUMERICAL INVESTIGATION OF A FISH ARTIFICIAL LATERAL LINE CANAL

Shriram B. Pillapakkam , Charlotte Barbier, Joseph A. C. Humphrey
Department of Mechanical and Aerospace Engineering
University of Virginia
Charlottesville, VA 22904, USA

Arne Rüter, Björn Otto, Horst Bleckmann
Institut für Zoologie, Universität Bonn, Poppelsdorfer Schloß
D-53115 Bonn

Wolf Hanke
Department of Organismic and Evolutionary Biology
Lauder Laboratory, Harvard University
Cambridge, MA 02138

ABSTRACT

Fish use the mechanosensory lateral line to detect water motions in their immediate surroundings and thus are able to avoid predators, track prey, swim in schools, and circumnavigate underwater objects. The basic unit of the lateral line is the neuromast, a sensory structure that consists of mechanosensitive hair cells enveloped in a gelatinous cupula. Lateral line neuromasts are distributed along the head and body of fish, either superficially on the skin or in subepidermal water-filled canals that open to the surroundings through a series of pores (Coombs et al. 1988). Water motions external to the fish induce pressure driven water motions inside the lateral line canal that drag on the cupulae of canal neuromasts causing them to be displaced by a few nanometers. These displacements, in turn, stimulate the underlying hair cells (Kalmijn 1988) which then signal the presence of the external water motions to the fish brain. Researchers have investigated fluid motions inside artificial lateral line canals (ALLCs) in response to sinusoidal external water motions to understand the functional significance of lateral line canals (LLCs). These studies have shown that LLCs behave like straight ALLCs of roughly the same cross sectional area. If an ALLC is stimulated in still water with a small-amplitude vibrating sphere placed adjacent to the canal, the water velocity inside the canal is proportional to the component of the external water acceleration that is parallel to the canal (Denton and Gray 1983). Up to now the filter properties of ALLCs have only been investigated in still water and only with a vibrating sphere as an external stimulus source. However, a fish may face a more complicated situation because either the fish moves, the water moves, or both move. We have conducted a collaborative investigation of this problem by performing numerical calculations at the University of Virginia and experimental measurements at the University of Bonn.

INTRODUCTION

Fish use the mechanosensory lateral line to detect weak water motions (Bleckmann, 1994). The lateral line of fish consists of superficial neuromasts distributed all over the head and body and of neuromasts embedded in cephalic and trunk lateral line canals (Coombs et al. 1988). External water displacements induce fluid displacements inside LLCs that stimulate lateral line neuromasts. Up to now the functional properties of corresponding ALLCs have only been studied with a vibrating sphere placed in still water close to the canal (Denton and Gray 1983). These studies reveal that water motions inside a given part of a LLC are linearly related to those in the medium adjacent to this part of the canal. The studies further show that for frequencies below about 80 Hz, the ratio of displacement inside the canal to that in the medium falls with frequency; that is, the displacement inside the canal follows the velocity in the medium. In addition, water displacements in a given length of the canal are proportional to the component of the external velocity that is parallel to the canal (Denton and Gray 1983).

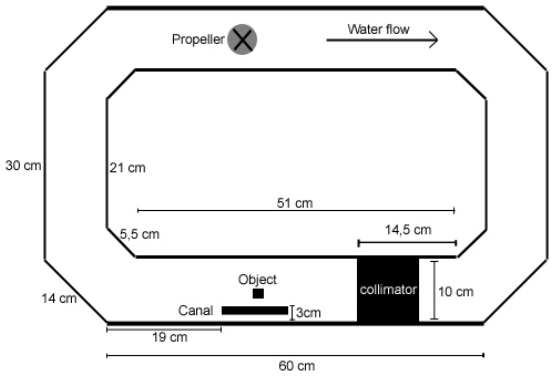

Fig. 1. Schematic of the water tunnel shown in plan view.

In the real world of fish the water often is not stationary. Instead many fish live in running water that often contains submerged objects that cause flow fluctuations and

pressure gradients, respectively. Fish use lateral line information to detect and localize submerged objects (Liao 2006). By analogy, it may be worthwhile to equip autonomous underwater vehicles with ALLCs capable of detecting hydrodynamic information for underwater navigation as well as for underwater object identification and tracking. To learn more about the functional properties of LLCs we have studied how vortical flows caused by a stationary cylinder placed in running water affect the motion of water inside an ALLC embedded in a fish model.

EXPERIMENTAL STUDY

We have studied the motions of water inside an ALLC embedded 1.5 mm into the flat side of a plastic fish model (canal length 10 cm, inner diameter 1 mm, number of pores 33, pore diameter 0.4 mm, interpore distance 3 mm). Measurements have also been made of the flow external to the ALLC, passing over the model as disrupted by the presence of a cylinder. The model (length 12.5 cm, height 5 cm, width 8 mm, with an in-plane curved head of radius 2.5 cm) was suspended vertically in a water flume and exposed to a conditioned uniform flow of velocity of 7 cm/s (±3%) (Fig. 1). Hydrodynamic biological-like stimuli were induced by vortex shedding from a cylinder (diameter 1 cm, length 10 cm) mounted normal to the external flow and parallel to the vertical model. The position of the cylinder was varied in the experiments (Fig. 2). At positions 1, 2a, and 3 the gap between the cylinder edge and the model was 1 cm. At positions 2b and 2c the gap was 2 and 3 cm, respectively. Light-scattering hollow glass spheres (Dantec), mostly of nominal diameter 50 μm, were used to track fluid motion inside the ALLC and past the fish model when exposed to the external hydrodynamic stimuli.

The water flow tank had a cross section of 10×15 cm^2, and the water height was 12 cm. The tank contained flow conditioning collimators upstream of the fish model. The flow was produced by a propeller (Schottelantrieb, Aeronaut 100) coupled to a d.c. motor (Conrad Electronic) that was driven by a power supply (Voltcraft, DIGI 35). The fish model was placed close (3 cm) and parallel to one of the side walls of the tank with its long axis also parallel to the incoming flow.

Quantification of internal flow

The pressure stimulus pathway to the interior of the ALLC canal was through a periodic array of pores. The bulk of the ALLC velocity data was obtained in the center of the canal where sphere displacements were largest. In this case, mean velocities were calculated by measuring the time taken for individual glass spheres (or an ensemble of spheres), filmed with a camera (OS 60D), to travel a distance of about 1.9 mm between adjacent canal pores.

Depending on the section of the canal investigated, the glass spheres showed oscillating motions u_2 superimposed on a steady unidirectional motion u_1. These oscillations were quantified by calculating an oscillation factor, OF, related to the rms of the u_2 velocity oscillations in the canal. To obtain the OF we measured the total distance (including the distances covered by any to and fro motions) the spheres moved after they had entered the left border of the camera field and until they reached the right border of the camera field. This total distance of sphere movement was

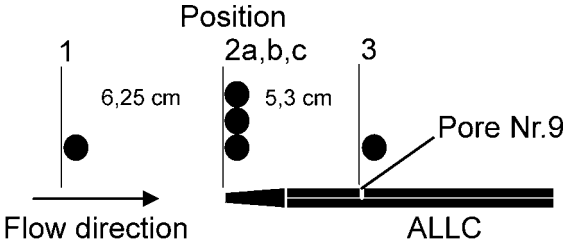

Fig. 2. Experimental test section. Filled circles indicate the positions of the cylinder with respect to the leading edge of the model (plan view). The curved head of the model points upstream. The posterior end of the model is streamlined with plasticine (not shown).

then divided by the width of the field of view. If a sphere did not leave the camera field (1.9 mm) within 10 s we measured the total distance it had traveled within these 10 seconds and divided this distance by the net distance the sphere had traveled. Assuming a sinusoidally oscillating flow of the form $u = u_1 + u_2 \sin(\omega t)$, for long time averages it can be shown that $OF \leq 0.9\ [u_2]_{rms}/u_1$ and, thus, OF provides an indirect measure of the local rms velocity normalized by the local constant velocity in the ALLC.

Quantification of external flow

Particle Image Velocimetry (PIV) (Lavision, Highspeedstar 4) was used to visualize and quantify the external water flow. Neutrally buoyant particles (Lavision, Sphericel 110P8), suspended in the water, were illuminated with a 1 mm thick light sheet generated with a laser (Pegasus 1 kHz, New Wave Research). The light sheet was oriented horizontally; that is, being contained in the x-y plane normal to both the cylinder and the fish model at the height of the ALLC (Figs. 2 and 5). Illuminated particles were filmed at a frame rate of 250 Hz for 8.2 s. Computations of PIV-images (vector plots, resolution: 85×85 vectors) were performed off-line with the software Davis 7 (LaVision). For a detailed description of the PIV calculations see Chagnaud et al. (2006).

Experimental Uncertainties

Due to their terminal velocity (~ 5 μm/s), at low flow velocities in the ALLC the particles were observed to sediment. To reduce this effect we quantified only the movements of particles that showed small vertical displacements and calculated only the horizontal component of particle motion.

The PIV-measurements revealed three problems: i) Because of light refraction, the cylinder used to generate vortical motions produced two regions of reduced light intensity to either side of it, one upstream and one downstream with respect to the approaching flow. The shadows were unavoidable because a horizontal laser sheet could only be generated with the aid of a mirror placed along the long axis of the model outside the flow tank. ii) Close to the edges and the glass walls of the test section illumination was not perfect, being too intense or too weak. iii) The camera had to be positioned directly above the model and, therefore, it registered some of the light scattered and reflected by the glass walls of the experimental tank. In areas where illumination was too weak or too intense the PIV produced false velocity data which were excluded from postprocessing.

RESULTS

Our measurements show that a cylinder (diameter 1 cm) placed near to an ALLC with an externally imposed flow induces complicated patterns of fluid motion external to and inside the ALLC. Irrespective of position, cylinder vortex shedding frequencies in the external flow at 7 cm/s are ~ 2 Hz. However, the patterns of flow inside the ALLC depend on the position of the cylinder relative to the fish model (Fig. 3 A-F). An artificial lateral line that is directionally sensitive not only can detect the velocity but also the direction of internal flow. The narrow spread of these oscillations (Fig. 3D-F) shows that there is little mechanical coupling between neighboring parts of the canal; that is, each short section of the canal behaves almost independently of neighboring sections. Thus the steady flow and the flow oscillations, respectively, in the ALLC not only indicate the presence but also the relative position (with respect to the long axis of the canal) of an external object.

The PIV data show that a cylinder placed adjacent to a fish model works to increase the external water velocity in the gap between the cylinder and the model that depends on cylinder diameter (data not shown) and gap size (Fig. 4).

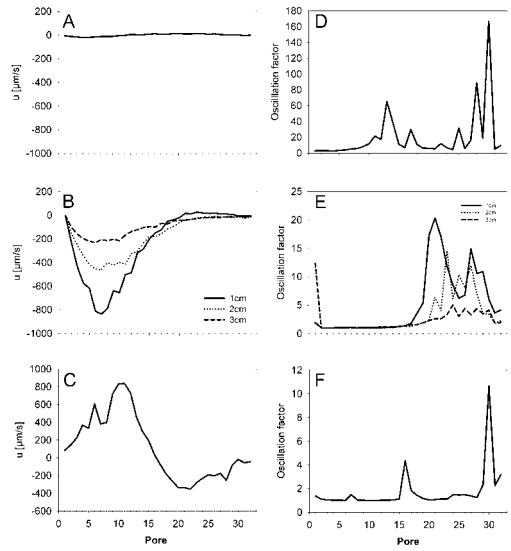

Fig. 3. A-F: Mean velocity u of glass spheres as a function of pore number for cylinder positions 1 (A), 2 a-c (B), and 3 (C) (Fig. 2). Glass sphere velocities are measured in the ALLC between adjacent pores. Cylinder diameter is 1 cm. The velocity of the external flow is 7 cm/s and its direction is from pore 1 to pore 33. Negative velocities inside the ALLC indicate sphere motions counter to the external flow direction. The plots in D, E and F show the corresponding oscillation factor, OF, as a function of pore number. Note differences in scales.

NUMERICAL METHOD

Fluid motion is described by continuity and momentum conservation equations appropriate to an unsteady, 2D, constant property flow expressed in Cartesian coordinates (Bird et al. 2002). The diameters of LLCs aligned along the length of fish are much smaller than the height of the fish and, therefore, it is reasonable to assume a 2D unsteady

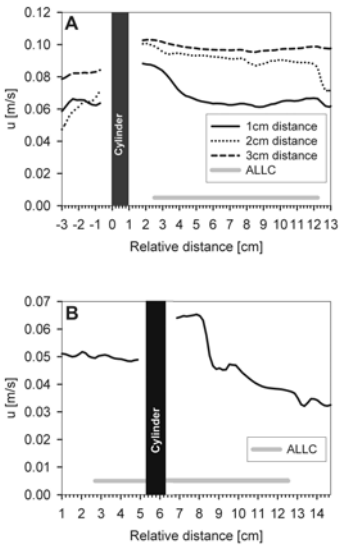

Fig. 4. Velocity measured in the horizontal plane at the height of the ALLC pores at a distance 5 mm from the model surface. Cylinder is placed at positions 1 (data not shown), 2 a-c (A), and 3 (B) (Fig. 2). Horizontal bar indicates position and length of the ALLC on the side of the model. Due to shadow effects particle motions close to the cylinder could not be measured.

external flow. The external flow numerical calculations are performed using the FAHTSO code (Rosales et al. 2000, 2001). This procedure solves finite difference forms of the conservation equations derived from control volume formulations on staggered grids for pressure and the three velocity components. Convection and diffusion terms are discretized using a third-order quadratic upwards interpolation scheme and a second-order central differencing technique, respectively. A fully implicit second order scheme is used for time. The procedure employs the SIMPLE algorithm described in (Patankar, 1980) in combination with the modified strongly implicit procedure to solve the system of algebraic finite difference equations.

The immersed boundary method (Peskin, 2002, Gilmanov et al., 2003) is adapted by tracking a set of discrete Lagrangian points that represent the surfaces of the ALLC and the cylinder. Once the Lagrangian grid points are established, the underlying Eulerian Cartesian grid is divided into: (i) Solid nodes that lie within the solid surfaces of the ALLC and the cylinder; (ii) Fluid nodes that lie in the fluid, at a certain distance away from solid surfaces; (iii) Immersed boundary nodes that lie in the fluid but close to solid surfaces. Homogeneous Dirichlet boundary conditions are applied for velocity and Neumann boundary conditions for pressure (to represent no-slip boundaries) at the discrete Lagrangian nodes. The values of primary variables at the immersed boundary nodes are computed by interpolating between known values of the variables at fluid nodes and points on the Lagrangian grid.

External flow

Unsteady 2D calculations were performed for the computational domain illustrated in Fig. 5 corresponding to the dimensions of the experimental test section. Flow was

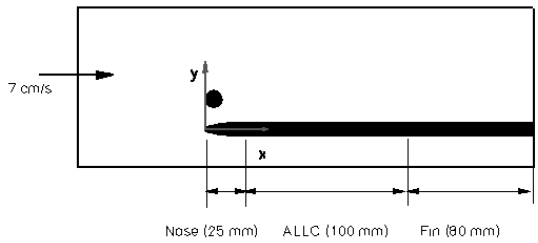

Fig. 5. Sketch to scale illustrating the domain for the external flow calculations. The ALLC starts 25mm from the fish model nose and the fin section extends 80mm past the ALLC portion of the model. In the experiments the fin section is made of plasticine and works to minimize vortex shedding from the model (and its attendant effects on the flow in the ALLC). Numerically the stabilizing effect of the fin was simulated by extending the model to the end of the computational domain as shown.

started from rest and a uniform velocity of 7 cm/s was imposed at the inlet plane. No-slip boundary conditions were applied at all surfaces and a developed flow condition was imposed at the exit plane. A non-uniform Cartesian grid with 572 × 202 nodes and a time-step of 2.5×10^{-3} s were used for all the calculations.

The value of pressure was monitored as a function of time at 33 pores (nodal points) set 3 mm apart as in the experiments. A plot of pressure versus time (not shown) allowed us to neglect the initial transient behavior and only the quasi-periodic data were considered for computing the flow inside the lateral line canal.

Internal flow

The water velocity inside the ALLC was estimated from Poiseuille's law using the external flow calculations of pressure as a function of time at the pores. Because the Reynolds number based on the canal diameter is very small (less than 1 in the experiments), the flow inside the canal is laminar. It is assumed that the flow varies slowly enough to use the steady state solution for each time step. Pressure is monitored at the first node above each pore and is used to derive the maximum velocity in the canal from the relation

$$u_{n+1/2} = -\frac{1}{4\mu}\frac{P_{n+1} - P_n}{\Delta x} R^2$$

where P_n is the pressure at pore n, Δx is the distance between two consecutive pores (3 mm) and R is the canal radius (0.5 mm). From these data we then obtained mean and rms values of velocity inside the ALLC.

RESULTS

Contours of the calculated external flow mean and rms velocities are shown in Figs. 6 and 7 with the corresponding PIV results for Case 2a. (Note that in the experiments measurements in the region between the cylinder and the nose of the fish model are ignored because of the shadow cast by the cylinder.) For both the experiments and the calculations the mean and rms velocities were obtained for the same length of time, 8.2 s.

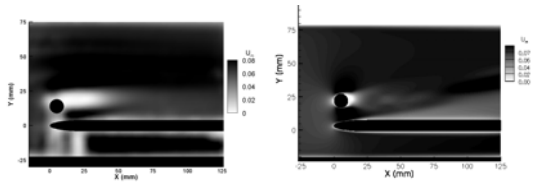

Fig. 6. Comparison between streamwise mean velocity (m/s) obtained in the experiments (left) and the calculations (right). In the experiments measurements between the cylinder and the leading edge of the model are ignored since this region falls in the shadow cast by the cylinder.

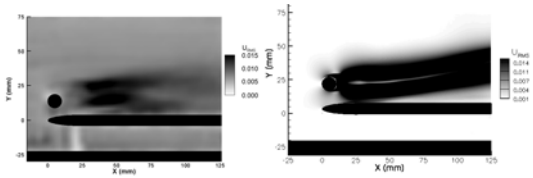

Fig. 7. Comparison between streamwise rms velocity (m/s) obtained in the experiments (left) and the calculations (right). In the experiments measurements between the cylinder and the leading edge of the model are ignored since this region falls in the shadow cast by the cylinder.

The experimental and numerical results agree in several respects in that both show: (i) a low velocity region just behind the cylinder; (ii) a high velocity region between the cylinder and the model; (iii) a boundary layer developing on the surface of the model; and (d) a region of high rms in the wake of the cylinder. In general, the rms in the experiments is higher than in the calculations. This is probably caused by the difficulty of obtaining a clean inlet velocity in the experiments. The boundary layer thickness at the end of the platform is much more pronounced in the calculations than in the experiments. This could be due to the inability of the boundary conditions used in the calculations to correctly simulate the outlet flow in the experiments. Figure 8 compares instantaneous measured and calculated contours of vorticity. In both cases the interaction between the wake and the boundary layer on the model can be seen, especially around x = 50 mm where a counter-rotating vortex is ejected from the boundary layer. This suggests that fish may use their lateral line to monitor their own boundary layer flow while simultaneously detecting external hydrodynamic stimuli.

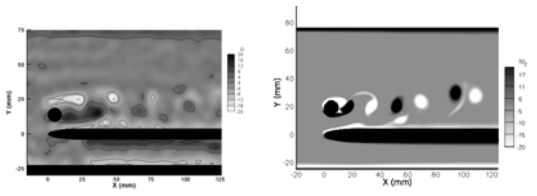

Fig. 8. Instantaneous vorticity (s^{-1}) contours from experiments (left) and calculations (right).

Calculations of the mean and rms velocities inside the ALLC are shown in Fig. 9. Some differences arise compared to the experiments but some interesting facts agree. In general, the mean and rms velocities are found to be significantly higher in the calculations than in the experiments. For Case 1 the calculations show a negative

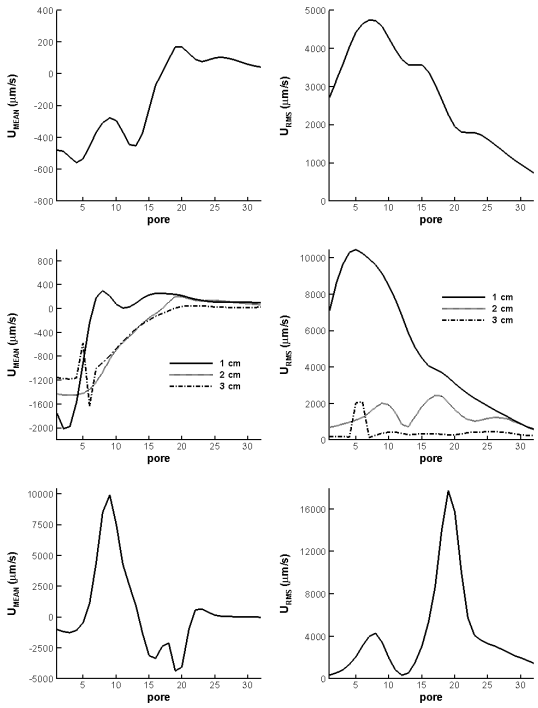

Fig. 9. Calculation of the mean (left) and rms (right) velocities inside the ALLC for Case 1 (top), 2a-c (middle) and 3 (bottom)

mean velocity in the ALLC along the first 15 pores, whereas the experiments show almost no velocity along the entire length of the ALLC. For Case 2, both calculations and experiments show negative mean velocity along the first half of the ALLC and almost no mean velocity for the second half. The calculations show high rms values in the first half of the ALLC for the case with the cylinder 1 cm away from the model due to the cylinder wake being nearer the ALLC. For Case 3, positive mean velocities are observed for both the calculations and experiments. However, the values are much larger for the calculations. More interestingly, the calculations show two rms maxima (pores 8 and 19) while the experiments show two OF maxima (pores 16 and 30). Some of the discrepancies observed between the ALLC numerical and experimental results may be partly due to the calculation assumption that pressure at a pore and at that pore location inside the ALLC have the same value. Since the canal is embedded 1.5 mm into the flat surface of the model there may be a loss of pressure along the 1.5 mm length of the pore.

Returning to the external flow, Fig. 10 shows wall pressure and shear stress distributions along the length of the model coinciding with the location of the ALLC. These results correspond to the plots of vorticity in Fig. 11 and are for times t_1 = 11 s and t_2 = 11.5 s in a flow at 7 cm/s with vortex shedding from the cylinder occurring at 2Hz. It is clear from the plots of P* that this quantity oscillates most strongly in terms of magnitude and slope along the first and second thirds of the ALLC, in broad agreement with the results in Figs. 3 and 9. Also, there is a strong correlation between the spatial-temporal variations of P* and τ* that suggests neuromasts external and internal to the LLC of a fish sense reinforcing hydrodynamic information

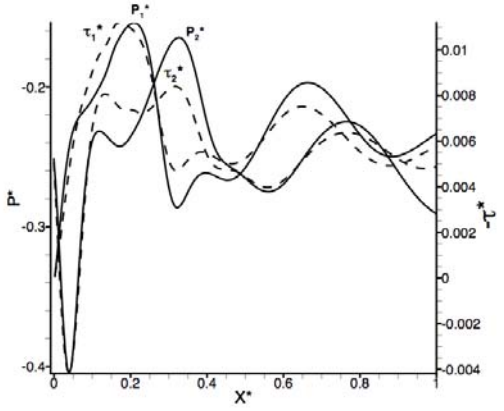

Fig. 10. Dimensionless wall pressure, $P_w/(1/2\rho U_{in}^2)$, and shear stress, $-\tau_w//(1/2\rho U_{in}^2)$ as a function of dimensionless distance along the length of the ALLC (U_{in} = 7cm/s, ρ = 977 kg/m^3). Curves labeled 1 are for t_1 = 11s and curves labeled 2 are for t_2 = 11.5s. Cylinder vortex shedding period is 0.5 s.

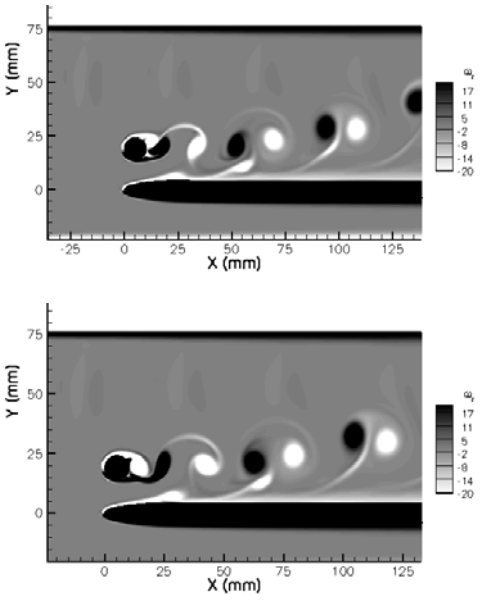

Fig. 11. Instantaneous contours of vorticity for the cylinder wake – model boundary layer flow interaction at t_1 = 11s (top) and t_2=11.5s (bottom) corresponding to the wall pressure and shear stress distributions of Fig. 10. Cylinder vortex shedding frequency is 2 Hz.

CONCLUSIONS

The present combined experimental and numerical investigation reveals some of the interactions that arise between the flow in the wake of a cylinder located near to a fish model and the flow inside the ALLC embedded in the model. In general, qualitative agreement is found between measurements and calculations. For the external flow, both the measurements and the calculations show that strong interactions arise between the wake of the cylinder and the boundary layer flow along the fish model. The pressure

fluctuations induced in the boundary layer by vortex shedding from the cylinder give rise to corresponding flow oscillations inside the ALLC. The magnitudes of the maxima of these oscillations and their location inside the ALLC correlate with the transverse and streamwise positions of the cylinder, respectively. This information is used by the LLC of fish to detect underwater objects fixed or moving relative to the fish.

ACKNOWLEDGMENTS

The authors gratefully acknowledge the financial support provided by DARPA BioSenSE AFOSR Grant #FA9550-05-1-0459 in support if this study. JACH expresses his sincere thanks to the University of Vienna where part of the work was performed while on sabbatical as a Guest Professor in the Department of Neurobiology and Cognition Research.

REFERENCES

Bird RB, Stewart WE, Lightfoot EN (2002) Transport Phenomena, John Wiley and Sons, Inc., New York

Bleckmann H (1994) Reception of hydrodynamic stimuli in aquatic and semiaquatic animals. In: Rathmayer W (ed) Progress in Zoology. Volume 41, 1 edn. Gustav Fischer, Stuttgart, Jena, New York, pp 1-115

Chagnaud BP, Bleckmann H, Engelmann J (2006) Neural responses of goldfish lateral line afferents to vortex motions. J.Exp.Biol. 209:327-342

Coombs S, Janssen J, Webb JF (1988) Diversity of lateral line systems: evolutionary and functional considerations. In: Atema J, Fay RR, Popper AN, Tavolga WN (eds) Sensory Biology of Aquatic Animals, 1 edn. Springer, New York, pp 553-593

Denton EJ, Gray JAB (1983) Mechanical factors in the excitation of clupeid lateral lines. Proceedings of the Royal Society of London B 218:1-26

Gilmanov A, Sotiropoulos F, Balaras E (2003) A general reconstruction algorithm for simulating flows with complex 3D immersed boundaries on Cartesian grids, J. Comput. Phy. 191: pp 660-669

Kalmijn AJ (1988) Hydrodynamic and acoustic field detection. In: Atema J, Fay RR, Popper AN, Tavolga WN (eds) Sensory Biology of Aquatic Animals, 1 edn. Springer, New York, pp 83-130

Liao JC (2006) The role of the lateral line and vision on body kinematics and hydrodynamic preference of rainbow trout in turbulent flow. J.Exp.Biol. 209:4077-4090

Patankar, S.V. (1980) Numerical Heat Transfer and Fluid Flow, Hemisphere Publishing Corporation, New York

Peskin, CS (2002) The immersed boundary method, Acta Numerica 11: pp 1: 479-517.

Rosales JL, Ortega A, Humphrey JAC (2000) A numerical investigation of the convective heat transfer in unsteady laminar flow past a single and tandem pair of square cylinders in a channel. Num. Heat Transfer, Part A 38: 443-465

Rosales JL, Ortega A, Humphrey JAC (2001) A numerical simulation of the convective heat transfer in confined channel flow past square cylinders: comparison of inline and offset tandem pairs," Int. J. Heat and Mass Transfer 44: 587-603